PAPER

Direct correlation between open-circuit voltage and quasi-fermi level splitting in perovskite solar cells: a computational step involving thickness, doping, lifetime, and temperature variations for green solutions

Muhammad Umar Salman, [ID] [a] Muhammad Mehak,[a] Umair Ali,[a] Ghulam Moin U Din,[a] Shahid M. Ramay,[b] M. Younis[c] and Shahid Atiq [ID] *[a]

In this study, a 1D perovskite-based solar cell was simulated using COMSOL, incorporating $CH_3NH_3GeI_3$ (organic in-organic hybrid) as an absorber layer, SnO_2 as the electron transport layer (ETL), and Cu_2Te as the hole transport layer (HTL). The simulations reveal that reducing the ETL's thickness enhances current density (J), although the maximum output power (P_{max}) diminishes with ETL's thickness. Conversely, increasing the absorber layer's thickness boosts open-circuit voltage (V_{oc}) and efficiency, exhibiting direct relation between V_{oc} and quasi-Fermi level splitting. Furthermore, variations in HTL thickness do not significantly affect V_{oc} or P_{max}. Notably, V_{oc} and P_{max} both increase with acceptor density, conversely, increase in donor density leads to declines in both V_{oc} and P_{max}. While extending the electron–hole (e–h) lifetime within the ETL results in marginal efficiency improvements, significant enhancements in the e–h lifetime within the absorber layer substantially improve performance. However, the efficiency remains unaffected by variations in the e–h lifetime of the HTL. Additionally, higher operating temperatures adversely impact device performance, reducing J, V_{oc}, P_{max}, fill factor, and overall efficiency. This study provides critical insights into optimizing material properties and device parameters for experimental applications, underscoring the potential of $CH_3NH_3GeI_3$-based perovskites as viable candidates for next-generation photovoltaic technologies.

1. Introduction

Global energy consumption has surged by over 50% in the past two decades, driving a corresponding rise in carbon dioxide emissions.[1] The energy sector fulfils more than 80% of global energy demand and contributes approximately 75% of greenhouse gas emissions worldwide.[2–4] With energy demand projected to grow by 25% in the coming years, renewable energy is expected to meet nearly 40% of the global supply by 2040, underscoring the critical need for sustainable solutions like solar energy.[5] Among renewable sources, solar energy has gained significant traction due to its abundance and capacity to meet a substantial portion of global energy needs. In particular, perovskite solar cells (PSCs) have garnered attention for their high efficiency, low production costs, and ease of fabrication,

with reported power conversion efficiencies (PCEs) reaching ~25.5%.[6,7] Approaching the performance of conventional silicon-based solar cells, PSCs represent a promising avenue for the global energy transition. The layered structure of PSCs comprises an electron transport layer (ETL), a perovskite absorber layer (PVK), and a hole transport layer (HTL), working synergistically to optimize light absorption and charge separation, critical for their efficiency and stability.[8,9]

The ETL plays a pivotal role in selectively transporting electrons from the PVK layer to the electrode while blocking holes, thereby minimizing recombination losses. Tin dioxide (SnO_2) is a widely used ETL material due to its high electron mobility, wide bandgap (~3.6 eV), and excellent optical transparency, enabling efficient electron conduction and sunlight penetration.[10–13] Additionally, SnO_2 offers superior thermal and chemical stability, can be fabricated at low temperatures, and resists degradation under UV exposure.[14–17] Its compatibility with diverse fabrication methods, including sputtering and solution processing, further enhances its versatility. Collectively, these properties significantly boost the stability and efficiency of PSCs.

[a]Centre of Excellence in Solid State Physics, University of the Punjab, Lahore-54590, Pakistan. E-mail: satiq@cssp.pu.edu.pk

[b]Physics and Astronomy Department, College of Science, King Saud University, P.O. Box 2455, Riyadh 11451, Saudi Arabia

[c]College of Physics and Optoelectronic Engineering, Shenzhen University, Shenzhen 518060, China

The PVK layer is the core of the solar cell, responsible for absorbing sunlight and generating electron–hole (e–h) pairs. For organic in-organic hybrid, lead (Pb)-free methylammonium germanium iodide ($CH_3NH_3GeI_3$) serves as a greener alternative to conventional perovskites, achieving PCE exceeding 18.01%.[18] Here, CH_3NH_3 is organic while Ge and I_3 are in-organic parts in PVK material. Its high absorption and optimal bandgap (~1.6 eV) facilitate efficient photon conversion across the visible spectrum.[19,20] Furthermore, $CH_3NH_3GeI_3$ offers long carrier diffusion lengths and high charge mobility, essential for reducing recombination losses and enhancing device performance.[21] It exhibits a favorable tolerance factor ($t = 0.97$), which lies within the empirical range of 0.97–1.03, making it an ideal perovskite candidate.[22] Although slightly distorted, this value is still considered within the acceptable margin for stable perovskite structures. Existing literature confirms the viability of $MAGeI_3$ in photovoltaic application, highlighting its distorted orthorhombic or tetragonal symmetry—structurally comparable to $MASnI_3$. In this context, various studies have explored the stability and electronic properties of Ge-based perovskites, identifying $MAGeI_3$ as a promising, lead-free alternative.[23–25]

After optimizing the lattice parameters *via* VESTA, the cubic perovskite unit cell of $CH_3NH_3GeI_3$'s crystal structure is generated, as shown in Fig. 1(a). This material strikes an ideal balance between sustainability and photovoltaic (PV) efficiency, making it a strong candidate for next-generation solar cells.

The HTL completes the charge separation process by extracting and transferring holes from the PVK layer to the electrode. Copper telluride (Cu_2Te) is a promising HTL material, offering high hole conductivity (>100 cm^2 V^{-1} s^{-1}), excellent thermal and chemical stability, and proper energy level alignment with the PVK layer.[26] Its high work function and p-type conductivity enhance hole extraction while minimizing recombination losses. Cu_2Te also boasts a simple binary composition, low toxicity, earth abundance, a direct bandgap of ~1.10 eV, and a notable absorption coefficient (>10^4 cm^{-1}).[27–30] These properties, coupled with its operational stability and scalability, make it a valuable component for improving the efficiency and longevity of PSCs.

In this study, we simulated 1D $SnO_2/CH_3NH_3GeI_3/Cu_2Te$ solar cell configuration observing the point ideal ohmic front and back contacts at room temperature. The SnO_2/CH_3NH_3-GeI_3/Cu_2Te configuration enhances PSC performance by maximizing charge transfer and reducing recombination losses. The precise energy band alignment among SnO_2, $CH_3NH_3GeI_3$ ($MAGeI_3$), and Cu_2Te, as shown in Fig. 1(b), is critical for optimizing charge dynamics and device performance. It can be seen that the energies of valence band (E_v), conduction band (E_c), electron fermi energy level (E_{fn}), and hole fermi energy level (E_{fp}) of each layer are well matching and ensuring the smooth pathway for the removal of electron and hole towards respective electrodes. SnO_2's wide bandgap prevents electron recombination and directs electrons toward the top contact, while the alignment between $MAGeI_3$ and Cu_2Te facilitates efficient hole transport. This well-engineered $SnO_2/CH_3NH_3GeI_3/Cu_2Te$ architecture achieves efficient photon absorption, charge separation, and carrier transport with minimal recombination losses, demonstrating the potential for high-performance solar energy conversion at room temperature. This design not only boosts device efficiency and stability but also addresses environmental concerns through the use of non-toxic materials, positioning it as a viable solution for sustainable and efficient solar energy generation.

2. Numerical modelling

The primary objective of a solar cell is to understand how light-generated charge carriers (electrons and holes) respond to internal electric fields.[31] The simulation process requires for solving three equations: the Poisson equation, the continuity equations for electrons and holes, and the current density (J) equations. Each equation plays a distinct role in characterizing the solar cell's overall behaviour. The Poisson equation (eqn (1) & (2)) governs the electrostatic potential generated by charge distribution within the device:

$$\frac{d^2\Psi(x)}{dx^2} = -\frac{p(x)}{\varepsilon} \quad (1)$$

$$\frac{dE}{dx} = -\frac{d^2\Psi(x)}{dx^2}$$
$$= \frac{q}{\varepsilon}\left[p(x) - n(x) + N_D^+(x) - N_A^-(x) + \rho_t(x) - n_t(x)\right] \quad (2)$$
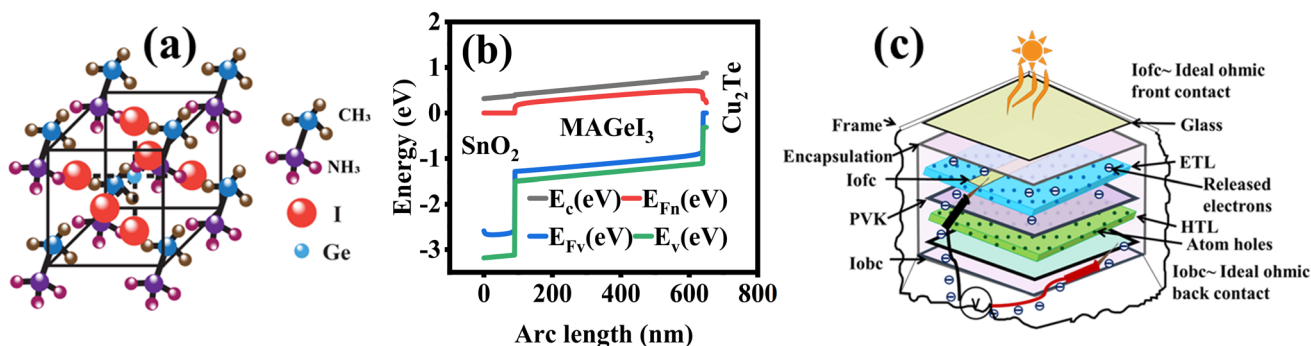

Fig. 1 (a) Crystal structure of $CH_3NH_3GeI_3$ perovskite material, (b) energy band alignment of ETL, PVK layer, and HTL to ensure the smooth pathway for removal of electron and hole from absorbing layer towards respective electrodes, and (c) schematic illustration of working of solar cell highlighting the role of thicknesses of ETL, PVK, and HTL.

Here in eqn (1) & (2), E represents electric field, Ψ denotes the electrostatic potential, q is the electron charge, and ε is the dielectric constant of the semiconductor material. The hole and electron concentrations are represented by p and n, respectively, while N_A^- and N_D^+ refer to the densities of ionized acceptors and donors, respectively. Additionally, ρ_t and n_t represent the concentrations of trapped holes and electrons, respectively, and x is the position coordinate within the material.[32] This formula connects the p–n junction parameter space charge with the electric field. The conservation of charge carriers in the device is described by the continuity equations (eqn (3) & (4)) for electrons and holes, which take into consideration the temporal and spatial fluctuations in carrier concentrations brought on by generation, recombination, diffusion, and drift in the electric field:

$$\frac{\partial J_n}{\partial x} + G - R = 0 \tag{3}$$

$$\frac{-\partial J_p}{\partial x} + G - R = 0 \tag{4}$$

Here, in eqn (3) & (4), for electrons, the generation and recombination rates are denoted by G and R, whereas the J is represented by J_n, while the comparable parameters for holes are represented as G, R, and J_p. These equations capture the charge carrier's movement and interaction under internal and external stimuli.[33,34] In eqn (5) & (6), J describes the combined effects of drift and diffusion on charge carrier flow:

$$J_n = qE_n\mu_n + qD_n\frac{\partial n}{\partial x} \tag{5}$$

$$J_p = qE_p\mu_p + qD_p\frac{\partial n}{\partial x} \tag{6}$$

Here, in eqn (5) & (6), q is the elementary charge, μ_n and μ_p are electron and hole mobilities, D_n and D_p are diffusion coefficients, and E is the electric field.[35,36] The equations highlight the interplay between the electric field and concentration gradients. The generation rate of carries due to light absorption is given by (eqn (7)):

$$G(x) = \alpha I_0 e^{-\alpha x} \tag{7}$$

Here, in eqn (7), I_0 is the incident light intensity (AM 1.5 standard spectrum is taken as reference here), α is the absorption coefficient, and x represents depth.[37] The exponential term describes the attenuation of light intensity as it penetrates the material. After generation of charge carriers, depending upon lifetime of these charge carrier, there happens recombination of charge carriers too. One of the types of recombination, there is Shockley–Read–Hall (SRH) recombination (and observed in this study), and it is given as (eqn (8)):

$$R = \frac{(np - n_0p_0)}{\tau_n(p + p_0) + \tau_p(n + n_0)} \tag{8}$$

This mechanism involves trap states or defects, with τ_n and τ_p denoting the lifetimes of electrons and holes.[38] There may be the probability of radiative recombination in working of solar cell, so it is given as (eqn (9)):

$$R = B(np - n_0p_0) \tag{9}$$

Photons are produced by the recombination of electrons and holes in direct-bandgap semiconductors. Recombination is dependent on the product of electron and hole concentrations (np) and their equilibrium values n_0p_0, and the radiative recombination coefficient is denoted by B.[39] These equations are discretized and solved over the geometry of the solar cell in COMSOL.[40] By solving these equations concurrently, COMSOL offers a comprehensive simulation of the solar cell's performance, including efficiency, current–voltage characteristics, and other crucial parameters. The optimized initial parameters for 1D $SnO_2/CH_3NH_3GeI_3/Cu_2Te$ solar cell are tabulated in Table 1.

3. Results and discussion

3.1 Effect of ETL thickness on solar cell performance

The ETL, PVK layer, and HTL are considered as pivotal layers in solar cell formation, and their thicknesses play a critical role in the output performance, as illustrated schematically in Fig. 1(c). The thinner ETL exhibits higher current densities due to efficient charge transport, as electrons generated in the absorber layer encounter minimal resistance while traversing the ETL. So, to analyze the effect of different ETL thicknesses on solar cell performance, it is varied from 10–90 nm, and current density–voltage (J–V) and power–voltage (P–V) characteristics are shown in Fig. 2(a). The P–V characteristics, indicating that

Table 1 The initial optimized parameters for 1D SnO_2 (ETL)/$CH_3NH_3GeI_3$ (PVK layer)/Cu_2Te (HTL) solar cell

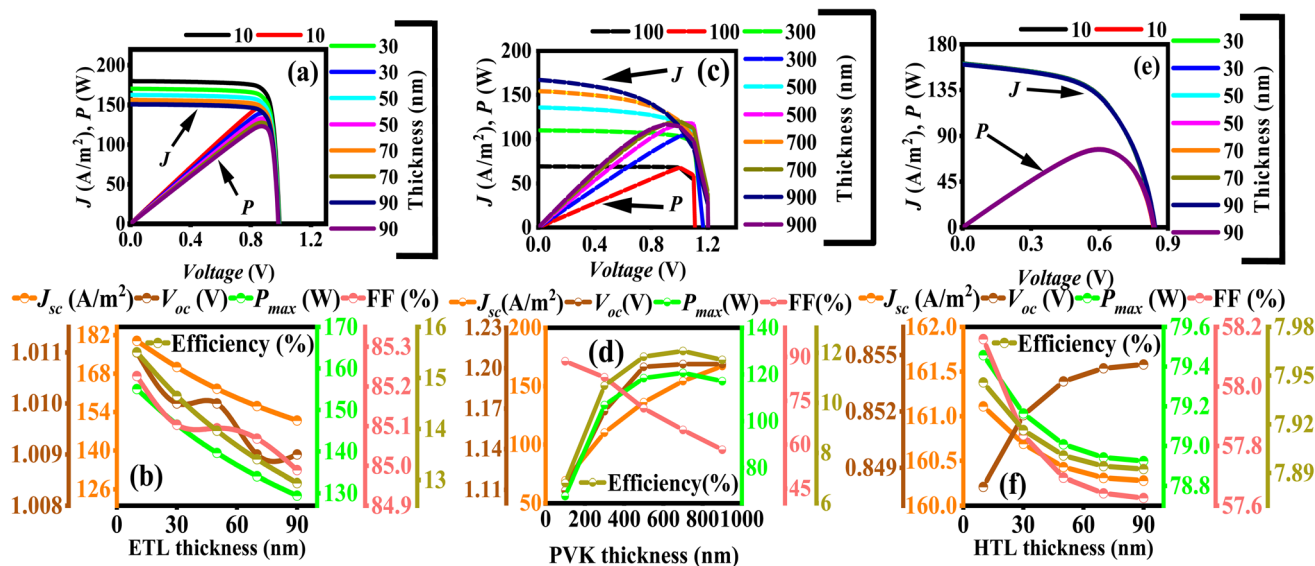| Parameters	ETL	PVK	HTL
Relative permittivity	10	10	10
Band gap (eV)	3.5	1.9	1.19
Electron affinity (eV)	4	3.98	4.1
Effective density of states, valence band (cm^{-3})	2.2×10^{19}	1×10^{16}	1.8×10^{19}
Effective density of states, conduction band (cm^{-3})	2.2×10^{18}	1×10^{15}	7.8×10^{17}
Electron mobility (m^2 V^{-1} s^{-1})	50	16.2	500
Hole mobility (m^2 V^{-1} s^{-1})	12	2.1	100
Electron lifetime, SRH (ns)	1000	1	1
Hole lifetime, SRH (ns)	1000	1	1

Fig. 2 (a) $J-V$ and $P-V$ characteristics at different ETL thicknesses (nm), and its effect on (b) J_{sc}, V_{oc}, P_{max}, FF, and efficiency, (c) $J-V$ and $P-V$ curves at different PVK thicknesses (nm), and its effect on (d) J_{sc}, V_{oc}, P_{max}, FF, and efficiency, (e) $J-V$ and $P-V$ response at different HTL thicknesses (nm), and its effect on (f) J_{sc}, V_{oc}, P_{max}, FF, and efficiency.

maximum power output (P_{max}) decreases with increasing ETL thickness due to resistive losses and recombination effects, which reduce optical transmittance and become more pronounced at higher voltages.[41,42] Fig. 2(b) present the variation in short-circuit current density (J_{sc}), open-circuit voltage (V_{oc}), P_{max}, fill factor (FF), and efficiency, showing that thinner ETLs (~10 nm) yield higher J_{sc} (179.940 A m^{-2}) due to reduced resistance and improved charge collection efficiency, enabling more photogenerated electrons to reach the contacts. The V_{oc} remains relatively constant (1.011 V at 10 nm and 1.009 at 90 nm) across a range of ETL thicknesses, as V_{oc} is primarily determined by material properties and energy level alignment at interfaces, with SnO$_2$ maintaining effective energy alignment irrespective of thickness. The P_{max} shows a significant decline (from 155.043–129.420 W) as ETL thickness increases (from 10–90 nm), driven by higher series resistance (R_s) and recombination losses associated with thicker ETLs, which impairs overall device performance. Similarly, the FF slightly declines (from 85.226–84.989%) with increasing ETL thickness due to rising R_s, which hampers efficient electron transport and reduces the device's ability to transmit power under ideal conditions. Finally, the power-dependent efficiency declines largely from

15.504% at 10 nm to 12.942% at 90 nm. Table 2 presents the detailed values of output characteristics of 1D SnO$_2$/CH$_3$NH$_3$-GeI$_3$/Cu$_2$Te solar cell at different ETL's thicknesses.

3.2 Effect of PVK thickness on solar cell performance

The $J-V$ characteristics reveal that thicker absorber layers enhance photon absorption, generating more e–h pairs and increasing J, as shown in Fig. 2(c).[43–46] However, beyond an optimal thickness (around 700 nm), resistive and recombination losses escalate, impairing charge collection efficiency and causing a decline in J, particularly at higher voltages. Similarly, the $P-V$ characteristics show that thicker layers improve absorption and charge generation, excessive thickness introduces resistive and recombination losses, reducing power output and illustrating the trade-off between absorption and recombination, as shown in Fig. 2(c). Fig. 2(d) shows that the J_{sc} increases (from 69.30–167.22 A m^{-2}) with absorber thickness (ranging from 100–900 nm), due to enhanced light absorption and charge carrier generation. However, as thickness increases, light absorption saturates, and additional thickness amplifies recombination rates, limiting effective charge collection, and consequently exhibits asymptotic behaviour beyond a certain thickness. In contrast, the V_{oc} initially rises with thickness (1.10 V at 100 nm and 1.20 V at 900 nm) due to improved light absorption and quasi-Fermi level splitting, exhibiting direct relation between V_{oc} and quasi-Fermi level splitting, as shown in Fig. 2(d). Nevertheless, V_{oc} saturates (~1.203 V) beyond a threshold thickness as resistive and recombination losses counterbalance further carrier generation gains. Moreover, Fig. 2(d) expresses that the P_{max} increases from 68.06 at 100 nm to 120.69 W at 700 nm but then starts to decline (117 W at 900 nm) due to elevated resistive and recombination losses. Furthermore, the FF diminishes as thickness increase (from

Table 2 The effect of ETL's thicknesses on output characteristics of 1D SnO$_2$/CH$_3$NH$_3$GeI$_3$/Cu$_2$Te solar cell

ETL thickness (nm)	J_{sc} (A m^{-2})	V_{oc} (V)	P_{max} (W)	FF (%)	Efficiency (%)
10	179.940	1.011	155.043	85.226	15.504
30	170.410	1.010	146.475	85.103	14.647
50	162.490	1.010	139.653	85.094	13.965
70	156.190	1.009	134.064	85.068	13.406
90	150.920	1.009	129.420	84.989	12.942

Table 3 The effect of PVK's thicknesses on output characteristics of 1D $SnO_2/CH_3NH_3GeI_3/Cu_2Te$ solar cell

PVK's thickness (nm)	J_{sc} (A m^{-2})	V_{oc} (V)	P_{max} (W)	FF (%)	Efficiency (%)
100	69.302	1.1094	68.0640	88.52859	6.8064
300	110.200	1.1680	106.8628	83.02371	10.6862
500	136.170	1.2010	118.4200	72.41034	11.8420
700	154.300	1.2030	120.6900	65.01892	12.0690
900	167.220	1.2030	117.1350	58.22813	11.7135

88.52% at 100 nm to 58% at 900 nm), as shown in Fig. 2(d), because higher resistive and recombination losses hinder the device's ability to operate near its optimal power point. Finally, the efficiency initially improves with absorber thickness (from 6.8 to 12.06% within 100 to 700 nm) due to enhanced light absorption and increased current generation, as shown in Fig. 2(d). However, efficiency saturates or marginally declines after beyond the optimal thickness of 700 nm, as recombination and resistive losses dominate. All these output characteristics of 1D $SnO_2/CH_3NH_3GeI_3/Cu_2Te$ solar cell at different PVK's thicknesses are listed in Table 3.

3.3 Effect of HTL thickness on solar cell performance

Fig. 2(e) presents the J–V characteristics at varied HTL thicknesses ranging from 10–90 nm, and demonstrate that thinner HTLs facilitate effective hole transport due to reduced resistance, resulting in higher J. As HTL thickness increases, resistance grows, elongating the hole transport path, which diminishes J and increases the likelihood of charge recombination.[44] Similarly, the P–V characteristics reveal that optimal HTL thickness (around 10 nm) achieves peak power output by minimizing resistive losses and recombination, while thicker HTLs (~90 nm) exhibit reduced power output due to increased R_s. Furthermore, Fig. 2(f) shows the variation in J_{sc}, V_{oc}, P_{max}, FF, and efficiency for different HTL thicknesses, elucidates that the J_{sc} reduces slightly from 161.110 A m^{-2} at 10 nm to 160.280 A m^{-2} at 90 nm, as photocarrier generation is governed by the absorber layer as well as HTL thickness. Marginal reductions (from 161.1 to 160.2 A m^{-2}) in J_{sc} at higher thicknesses (~90 nm) result from slight resistance and recombination losses, though these effects are negligible. The V_{oc} slightly increases (from 0.8480 V at 10 nm to 0.8545 V at 90 nm) since the HTL primarily facilitates hole transport and electron blocking, without affecting the absorber's properties and it varies P_{max}

(~79.458–78.924 W) under HTL thicknesses. Similarly, the FF reduces lightly (58.159–57.625%), as the HTL balances R_s and shunt resistance (R_{sh}). Neither overly thin nor thick HTLs dominate in this range, maintaining effective charge extraction and transport. Finally, likewise P_{max}, the efficiency follows the same decreasing trend (ranging from 7.945% at 10 nm to 7.892% at 90 nm) across the HTL thickness range, as it directly co-relates with the stable V_{oc}, J_{sc}, and FF. The comprehensive numerical output characteristics of 1D $SnO_2/CH_3NH_3GeI_3/Cu_2Te$ solar cell at different HTL's thicknesses are enlisted in Table 4.

3.4 Effect of acceptor concentration on solar cell performance

At lower voltages, J improves with higher acceptor density (N_A) due to increased charge carrier concentration in the p-type region, which strengthens the electric field in the depletion region. This stronger field facilitates the separation of photogenerated e–h pairs, reducing recombination losses and enhancing J, as shown schematically in Fig. 3(a). The J–V and P–V characteristics at different N_A (ranging from 1×10^{15} to 1×10^{20} cm^{-3}) for HTL layer, are shown in Fig. 3(b).[47–49] The stronger electric field in the depletion region accelerates the separation of photogenerated carriers, further reducing recombination and R_s, leading to linear growth in J_{sc} (from 160.35 at 1×10^{15} to 172.23 A m^{-2} at 1×10^{20} cm^{-3}), as shown in Fig. 3(c). Moreover, Fig. 3(c) shows that V_{oc} rises (from 0.95 to 1.27 V) with N_A as the strengthened electric field enhances quasi-Fermi level splitting, intrinsic potential, and charge carrier separation while minimizing recombination and R_s. The P_{max} significantly improves (79.36 to 122.64 W) with increasing N_A, as shown in Fig. 3(c), as the enhanced electric field optimizes the separation and collection of photogenerated carriers, reducing recombination losses and boosting J and voltage. However, Auger recombination and increased R_s may limit further gains at very high doping level. Additionally, Fig. 3(c) presents the FF and efficiency, showing that the FF also rises steadily (52–56%) with N_A, as improved intrinsic potential and reduced recombination losses enhance carrier collection efficiency and conductivity. Similarly, efficiency increases approximately linearly (7.9–12.2%) with N_A due to enhanced V_{oc}, J_{sc}, and FF, which result from improved charge carrier extraction and reduced recombination. At very high doping levels, efficiency gains may plateau or decline slightly due to increased resistive losses and carrier–carrier interactions such as Auger recombination. Overall, higher N_A enhances materials

Table 4 The effect of HTL's thicknesses on output characteristics of 1D $SnO_2/CH_3NH_3GeI_3/Cu_2Te$ solar cell

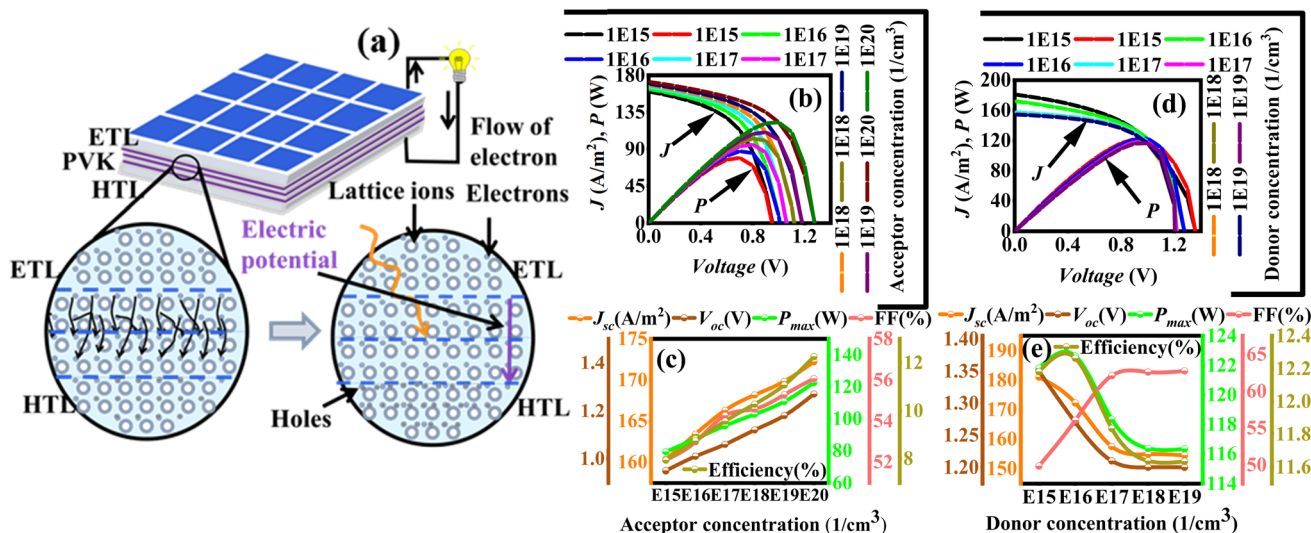| HTL thickness (nm)	J_{sc} (A m^{-2})	V_{oc} (V)	P_{max} (W)	FF (%)	Efficiency (%)
10	161.110	0.8480	79.458	58.159	7.945
30	160.690	0.8518	79.164	57.836	7.916
50	160.430	0.8536	79.008	57.694	7.900
70	160.310	0.8543	78.942	57.641	7.894
90	160.280	0.8545	78.924	57.625	7.892

Fig. 3 (a) Schematic illustration exhibiting the role of donor/acceptor concentrations of ETL and HTL on solar cell performance, (b) $J–V$ and $P–V$ characteristics at different acceptor concentrations, and its effect on (c) J_{sc}, V_{oc}, P_{max}, FF, and efficiency, (d) $J–V$ and $P–V$ curves at different donor concentrations, and its effect on (e) J_{sc}, V_{oc}, P_{max}, FF, and efficiency.

Table 5 The effect of acceptor concentrations (N_A) on output characteristics of 1D SnO$_2$/CH$_3$NH$_3$GeI$_3$/Cu$_2$Te solar cell

N_A (cm^{-3})	J_{sc} (A m^{-2})	V_{oc} (V)	P_{max} (W)	FF (%)	Efficiency (%)
1×10^{15}	160.35	0.95	79.366	52.10050	7.9366
1×10^{16}	163.41	1.01	87.451	52.98644	8.7451
1×10^{17}	166.31	1.06	95.680	54.27464	9.5680
1×10^{18}	168.18	1.12	102.816	54.58437	10.2816
1×10^{19}	169.84	1.18	110.799	55.28583	11.0799
1×10^{20}	172.23	1.27	122.640	56.06859	12.2640

conductivity and reduces R_s, optimizing solar cell performance within the observed range. Table 5 presents the detailed values of all output characteristics at different N_A for 1D SnO$_2$/CH$_3$NH$_3$GeI$_3$/Cu$_2$Te solar cell.

3.5 Effect of donor concentration on solar cell performance

The $J–V$ and $P–V$ characteristics at varying donor concentrations (N_D) from 1×10^{15} to 1×10^{19} cm^{-3}, as shown in Fig. 3(d), to check their effects on solar cell performance.[50] Fig. 3(e) presents the variation in J_{sc}, V_{oc}, P_{max}, FF, and efficiency at different N_D, explaining that the J_{sc} abruptly decreases from 181.03 at 1×10^{15} to 154.89 A m^{-2} at 1×10^{18} cm^{-3}, and then saturation

Table 6 The effect of donor concentrations (N_D) on output characteristics of 1D SnO$_2$/CH$_3$NH$_3$GeI$_3$/Cu$_2$Te solar cell

N_D (cm^{-3})	J_{sc} (A m^{-2})	V_{oc} (V)	P_{max} (W)	FF (%)	Efficiency (%)
1×10^{15}	181.03	1.35	121.815	49.84441	12.1815
1×10^{16}	172.23	1.27	122.64	56.06859	12.264
1×10^{17}	157.48	1.21	118.35	62.10942	11.835
1×10^{18}	154.89	1.2	116.37	62.60895	11.637
1×10^{19}	154.47	1.2	116.34	62.76300	11.634

trend follows ($\sim$154.47 A m^{-2}). At lower N_D, J_{sc} increases rapidly due to enhanced carrier generation and separation driven by a stronger electric field. As N_D rises further, the electric field becomes sufficiency to collect most carriers, causing J_{sc} to saturate. Similarly, V_{oc} declines as N_D increases (from 1.35 to 1.21 V in the range of 1×10^{15}–1×10^{17} cm^{-3}), because at lower N_D, a wider depletion region creates a stronger electric field and higher built-in potential. As N_D rises, the depletion width narrows, and junction recombination increases, slightly reducing V_{oc}. Beyond a certain N_D, V_{oc} stabilizes as the built-in potential saturates ($\sim$1.2 V). However, the P_{max} is high for lower N_D and it reduces sharply as the densities increase (from 121.81 at 1×10^{15} to 116.34 W at 1×10^{19} cm^{-3}). Moreover, the FF increases at low N_D, where high R_s limits current delivery efficiency. As N_D rises, R_s decreases, improving carrier collection and FF (49.84–62%). On the other hand, the efficiency initially declines (from 12.18 to 11.63%) slightly before stabilizing as N_D increases. Table 6 shows the all-output parameters of 1D SnO$_2$/CH$_3$NH$_3$GeI$_3$/Cu$_2$Te solar cell for varying N_D.

3.6 Effect of ETL electron–hole (e–h) lifetime on solar cell performance

It is obvious that the photo-induced charge carriers have lifetime at nanoscale, which may be longer or shorter depending upon the incident light and material's properties. If carriers have shorter lifetime, it may increase the recombination losses, while on the other hand, there is greater probability of low recombination if charge carriers have longer lifetime. In this case, due to longer life span, the charge carriers may have enough time from the creation to collection at electrodes, and contribute to the enhanced performance of solar cell. Fig. 4 shows that there are two red and blue spheres labelled as having shorter and longer lifetimes, respectively, where red spheres are unable to be collected at respective electrode. Fig. 5(a) shows the
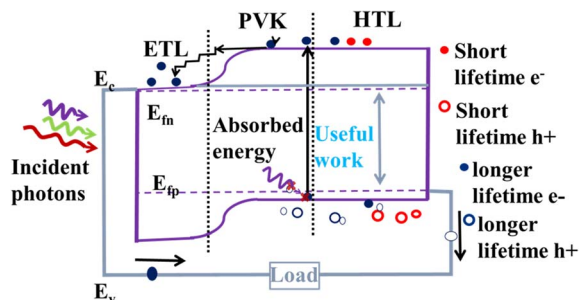
Fig. 4 Schematic illustration exhibiting the role of e−h lifetime of ETL, PVK, and HTL on solar cell perform.

Table 7 The effect of ETL's electron–hole (e–h) lifetime on output characteristics of 1D SnO$_2$/CH$_3$NH$_3$GeI$_3$/Cu$_2$Te solar cell

ETL's e–h lifetime (ns)	J_{sc} (A m^{-2})	V_{oc} (V)	P_{max} (W)	FF (%)	Efficiency (%)
1	172.23	1.27	122.64	56.06859	12.264
10	173.37	1.28	123.55	55.67482	12.355
100	173.49	1.28	123.64	55.67684	12.364
1000	173.5	1.27	123.65	56.11654	12.365

J–V and P–V characteristics in lifetime range of 1–1000 ns, revealing that increasing e–h lifetimes enhance current at a given voltage by reducing recombination losses, resulting in steeper curves and improved carrier collection efficiency.[51–54] Similarly, the P–V characteristics show that the maximum power point shifts to higher voltages as power output rises with extended lifetimes, due to more carriers contributing to both current and voltage. This leads to a higher J_{sc} (172.23–173.5 A m^{-2}) as longer lifetimes allow more carriers to be captured before recombining, as shown in Fig. 5(b). Furthermore, Fig. 5(b) represents the V_{oc} also increases (1.27–1.28 V) with e–h lifetime (1–100 ns), but after 100 ns, it starts to reduce again. Moreover, the P_{max} improves (from 122.64 to 123.65 W) with longer lifetimes as reduced recombination enables more carriers to generate power, plateauing near optimal efficiency. Additionally, Fig. 5(b) shows FF and efficiency measurements, expressing that the FF slightly decreases from 56 to 55% but then starts to achieve again 56% at higher lifetime (∼1000 nm). Overall, efficiency, which depends on V_{oc}, J_{sc}, and FF, rises from 12.26 to 12.36% with e–h lifetime as recombination losses diminishes, eventually stabilizing (∼12.36%) near the theoretical maximum efficiency. Table 7 summarizes the output parameters at varying e–h lifetimes for ETL in 1D SnO$_2$/CH$_3$-NH$_3$GeI$_3$/Cu$_2$Te solar cell.

3.7 Effect of PVK electron–hole lifetime on solar cell performance

Fig. 5(c) presents the J–V and P–V characteristics across various e–h lifetimes (1–1000 ns), revealing that longer lifetimes reduce recombination losses, resulting in improved J_{sc} and steeper curves near the V_{oc}.[55] Furthermore, the P–V characteristics, showing that the maximum power point shifts to higher voltage and power values as carrier mobility improves and recombination decreases. The J_{sc} increases from 173.5 to 182.14 A m^{-2} with lifetime (1–1000 ns), and after this it may saturate, as shown in Fig. 5(d), due to enhanced carrier collection efficiency, reflecting near-intrinsic performance. Additionally, Fig. 5(d) presents that the V_{oc} rises with lifetime (1.28–1.31 V), and attains the saturation afterwards, driven by better quasi-Fermi level separation and reduced energy losses. Similarly, the P_{max} increases significantly at shorter lifetimes (from 123.65 W at 1 ns to 166.88 W at 1000 ns), saturating for longer durations as recombination losses decline. Moreover, the FF gradually rises (55–69%), as shown in Fig. 5(d), reflecting reduced energy losses and improved charge transport. The efficiency rapidly improves (12.36–16.68%) at shorter lifetimes and plateaus at 16.6%, as shown in Fig. 5(d), indicating optimal performance from cumulative enhancements in V_{oc}, J_{sc}, FF, and P_{max}, with
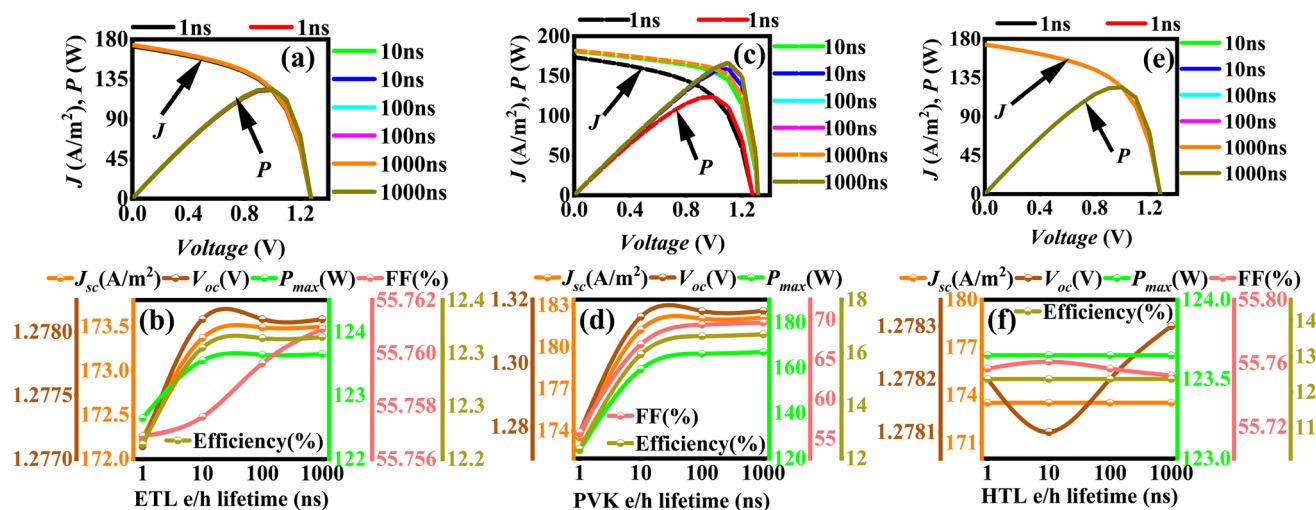

Fig. 5 (a) J–V and P–V characteristics at different e−h lifetime (ns) in ETL, and its effect on (b) J_{sc}, V_{oc}, P_{max}, FF, and efficiency, (c) J–V and P–V curves at different e−h lifetime (ns) in PVK, and its effect on (d) J_{sc}, V_{oc}, P_{max}, FF, and efficiency, (e) J–V and P–V response at different e−h lifetime (ns) in HTL, and its effect on (f) J_{sc}, V_{oc}, P_{max}, FF, and efficiency.

Table 8 The effect of PVK's electron–hole (e–h) lifetime on output characteristics of 1D SnO$_2$/CH$_3$NH$_3$GeI$_3$/Cu$_2$Te solar cell

PVK's e–h lifetime (ns)	J_{sc} (A m^{-2})	V_{oc} (V)	P_{max} (W)	FF (%)	Efficiency (%)
1	173.50	1.28	123.650	55.67813	12.3650
10	181.23	1.31	159.269	67.08569	15.9269
100	182.04	1.31	166.166	69.67934	16.6166
1000	182.12	1.31	166.881	69.94843	16.6881

diminishing returns beyond a certain lifetime. This behaviour underscores PVK's intrinsic efficiency potential and high–performance operation. Table 8 presents the output characteristics at varying e–h lifetimes for PVK layer in 1D SnO$_2$/CH$_3$NH$_3$GeI$_3$/Cu$_2$Te solar cell.

3.8 Effect of HTL electron–hole lifetime on solar cell performance

Fig. 5(e) depicts the J–V and P–V characteristics at different e–h lifetimes (1–1000 nm), highlighting the impact of recombination in Cu$_2$Te (HTL).[56–58] At shorter lifetimes, strong recombination significantly reduces current at higher voltages, whereas longer lifetimes dimmish recombination losses, allowing more charge carriers to reach the electrodes. Moreover, the P–V characteristics, revealing that short e–h lifetimes (1 ns) result in low power output due to its high recombination in the HTL. Fig. 5(f) shows the variation in J_{sc}, V_{oc}, P_{max}, FF, and efficiency, explaining that the J_{sc} remains relatively constant ($\sim$173.5 A m^{-2}) across different lifetimes because HTL's high conductivity minimizes recombination, even at shorter lifetimes, allowing most photogenerated carriers to contribute to the current. The stability of J_{sc} indicates its dependence on the active layer's light absorption and Cu$_2$Te's intrinsic properties, which ensure efficient hole extraction and transport regardless of lifetime variations. The V_{oc} changes in the range of 1.27–1.28 V with e–h lifetime, as longer lifetimes reduce recombination losses, enabling better charge separation and preservation. Short lifetimes result in fewer available carriers, lowering V_{oc}, while longer lifetimes (*e.g.*, 1000 ns) allow V_{oc} to reach its maximum due to Cu$_2$Te's ability to suppress recombination through efficient hole transport. Similarly, the P_{max} also remains invariant and achieves 123.65 W at all lifetime values. Furthermore, the FF follows same trend as V_{oc} is behaving in this measurement but the efficiency remains relatively stable ($\sim$12.36%) across different e–h lifetimes. The output characteristics at varying e–h lifetimes for HTL in 1D SnO$_2$/CH$_3$NH$_3$GeI$_3$/Cu$_2$Te solar cell are tabulated in Table 9.

Table 9 The effect of HTL's electron–hole (e–h) lifetime on output characteristics of 1D SnO$_2$/CH$_3$NH$_3$GeI$_3$/Cu$_2$Te solar cell

HTL's e–h lifetime (ns)	J_{sc} (A m^{-2})	V_{oc} (V)	P_{max} (W)	FF (%)	Efficiency (%)
1	173.5	1.27	123.65	56.11654	12.365
10	173.5	1.28	123.65	55.67813	12.365
100	173.5	1.27	123.65	56.11654	12.365
1000	173.5	1.28	123.65	55.67813	12.365

In the lifetime variational study, both front and back contacts were assumed to be ohmic to minimize interfacial resistance, but the carrier lifetime remains a crucial factor influencing solar cell performance. Simulating carrier lifetime is essential because it affects recombination rates and ultimately impacts current density and fill factor. Even with ohmic contacts, charge carriers must pass through ETL and HTL, where short lifetimes can lead to significant recombination losses. Additionally, lifetime simulations provide insight into defect-related trap-assisted recombination mechanisms within the device layers. By incorporating carrier lifetime into COMSOL simulations, we ensured more realistic modeling of charge transport and efficiency, avoiding overly idealized results.

Furthermore, in this study, we examined the impact of carrier lifetime as a means to understand the influence of defect density on solar cell performance. Defect density is closely linked to carrier lifetime and significantly affects recombination dynamics and quasi-Fermi level splitting, ultimately influencing the V_{oc}. While in this study, there is no explicit simulation of defect density, its effects were captured indirectly through lifetime and recombination rate simulations, aligning with realistic experimental conditions.

3.9 Effect of temperature on solar cell performance

It is a common misconception that higher temperatures enhance solar energy generation; however, in reality, the opposite is true. As the temperature rises, the kinetic energy of photo-generated charge carriers increases, which in turn elevates the rate of recombination. This enhanced recombination diminishes the separation efficiency of electron–hole pairs, ultimately leading to a reduction in the overall efficiency of the solar cell. Fig. 6(a) illustrates this phenomenon, where two solar panels are depicted under different thermal conditions. The panel exposed to elevated temperatures is associated with a red battery icon in the bottom left corner, indicating lower power output. In contrast, the panel operating at a lower, more optimal temperature is accompanied by a green battery icon, signifying higher energy retention and efficiency. This visual representation effectively highlights the adverse impact of high temperature on solar cell performance. The J–V and P–V characteristics between 285–320 K, as shown in Fig. 6(b), revealing the output behaviour of solar cell. The V_{oc} decreases with rising temperature due to a narrowing bandgap and increased charge carrier recombination, which reduces the built-in potential and net carrier density. In this study, a narrow temperature range (35 K) was chosen deliberately to simulate realistic operational fluctuations that PVK solar cells, such as CH$_3$NH$_3$GeI$_3$, would
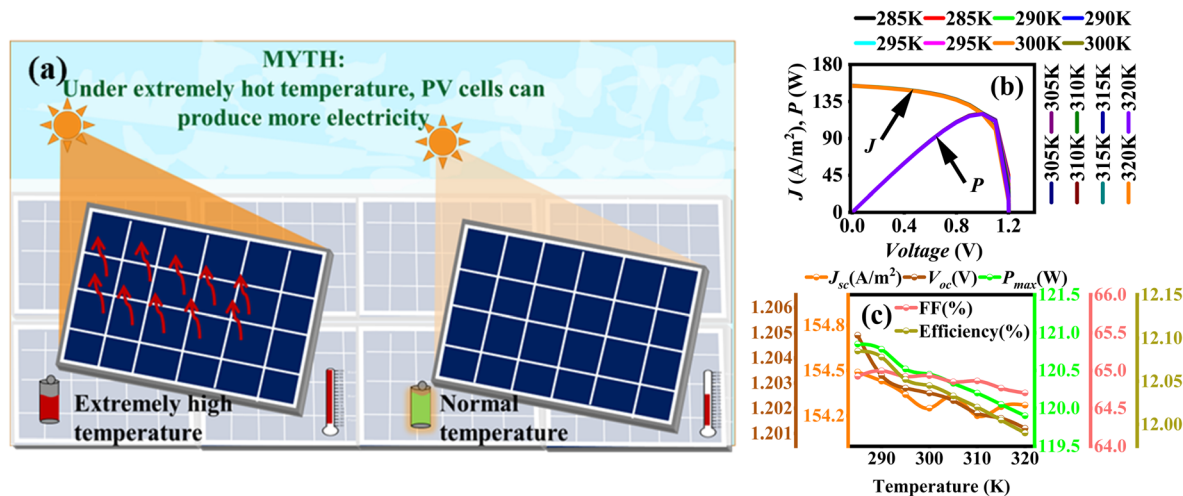
Fig. 6 (a) Visual representation of impact of lower and higher temperature (K) on solar cell performance, (b) J–V and P–V characteristics at different device's operating temperature (K), and its effect on (c) J_{sc}, V_{oc}, P_{max}, FF, and efficiency.

experience under near-ambient terrestrial conditions. This approach allowed to observe how practical temperature variations affect key parameters like quasi-Fermi level splitting, J_{sc}, V_{oc}, FF, and efficiency.

Fig. 6(c) presents the J_{sc}, V_{oc}, P_{max}, FF, and efficiency, revealing that the J_{sc} marginally decreases with temperature (from 154.49 at 285 K to 154.27 A m^{-2} at 320 K), reflecting the dominance of recombination over thermal carrier generation and potential material or interfacial degradation, while V_{oc} and P_{max} reduce negligibly at higher temperatures. Similarly, the FF also declines (from 65.02 to 64.71% in range of 285–320 K), due to increased resistive losses in the SnO$_2$ and Cu$_2$Te transport layers, while overall efficiency drops from 12.08 to below 12.00%, driven by reduced V_{oc}, P_{max}, and FF.[59,60] These trends highlight the sensitivity of CH$_3$NH$_3$GeI$_3$-based solar cells to temperature variations and emphasize the need for effective thermal management to maintain optimal performance. The effect of temperature on output characteristics of 1D SnO$_2$/CH$_3$NH$_3$GeI$_3$/Cu$_2$Te solar cell is summarized numerically in Table 10.

This study simulated key parameters—layer thicknesses, doping concentrations, carrier lifetimes, and temperature

variations—to optimize the performance of a PVK solar cell. The thickness of ETL, PVK, and HTL layers was systematically varied to balance light absorption, charge transport, and recombination losses; overly thick ETL/HTL layers can increase series resistance and reduce efficiency. Doping concentration were adjusted to fine-tune the built-in electric field, improve energy level alignment, and enhance carrier extraction. Carrier lifetime was analyzed as a measure of recombination, with longer lifetimes indicating better charge collection and fewer losses due to trap-assisted recombination. Simulating a range of lifetimes also provided insights into how defect densities affect device efficiency. Temperature variations were considered to reflect real-world conditions, as elevated temperatures increase recombination and internal resistance, degrading performance. A narrow realistic temperature range was chosen to evaluate thermal stability without extending beyond the intended scope of the study.

CH$_3$NH$_3$GeI$_3$ is a promising lead-free perovskite, but its performance is currently limited by sub-optimal band alignment, high defect densities, and degradation due to moisture sensitivity of Ge-based materials. These issues lead to reduced charge extraction, increased recombination, and compromised long-term stability. Additionally, fabrication challenges, particularly in interface engineering, hinder consistent device optimization.

Table 10 The effect of device's operating temperature on output characteristics of 1D SnO$_2$/CH$_3$NH$_3$GeI$_3$/Cu$_2$Te solar cell

Temperature (K)	J_{sc} (A m^{-2})	V_{oc} (V)	P_{max} (W)	FF (%)	Efficiency (%)
285	154.49	1.203	120.85	65.02504	12.085
290	154.43	1.202	120.78	65.06672	12.078
295	154.34	1.201	120.52	65.01860	12.052
300	154.25	1.200	120.45	65.07293	12.045
305	154.33	1.200	120.33	64.97441	12.033
310	154.20	1.197	120.20	65.12173	12.020
315	154.26	1.201	120.05	64.79863	12.005
320	154.27	1.201	119.90	64.71347	11.990

4. Conclusion

The escalating global challenges of climate change and dependence on environmentally hazardous energy sources have catalyzed the pursuit of sustainable and eco-friendly energy solutions. Among these, solar energy has emerged as a highly efficient, and over the past decades, extensive research has focused on developing advanced materials. In this regard, organic in-organic hybrid perovskite (PVK) materials, particularly CH$_3$NH$_3$GeI$_3$, have garnered substantial interest as

absorber layers due to their exceptional multifunctional properties. For this PVK material, using COMSOL, the 1D SnO$_2$/CH$_3$NH$_3$GeI$_3$/Cu$_2$Te solar cell is simulated. The study revealed that performance of solar cell is critically influenced by the thicknesses of electron transport layer (ETL), PVK layer, and hole transport layer (HTL), as well as by doping concentrations, carrier lifetimes, and device's operating temperature. Thinner ETLs ($\sim$10 nm) yield higher current densities, enhanced power output, and superior efficiency, whereas thicker ETLs exhibit diminishing performance. Similarly, the PVK layer achieves optimal performance at $\sim$700 nm, balancing photon absorption and charge collection efficiency, with efficiency declining beyond thickness. Specifically, open-circuit voltage (V_{oc}) enhances as the PVK layer's thickness increases due to quasi-Fermi level splitting, expressing the direct relation between V_{oc} and quasi-Fermi level splitting. Moreover, HTL thicknesses near 10 nm facilitate effective hole transport with minimal resistive losses, maintaining stable power and efficiency, while thicker HTLs ($\sim$90 nm) introduce minor performance declines. Furthermore, adjustments in acceptor and donor concentrations (N_A, N_D) significantly influence carrier dynamics, with higher N_A enhancing short-circuit current density (J_{sc}), V_{oc}, and efficiency, whereas higher donor densities stabilize performance but induce saturation trends in J_{sc} and V_{oc}. Additionally, extending electron–hole (e–h) lifetimes from 1–1000 ns markedly improves J_{sc}, V_{oc}, and power output (P_{max}). Finally, the overall performance including J_{sc}, V_{oc}, P_{max}, fill factor, and efficiency reduce as temperature increases (285–320 K). This study aids for optimizing material properties and device parameters for experimental purposes and encourages the potential of CH$_3$NH$_3$GeI$_3$-based perovskite materials as potential candidates for next-generation photovoltaic applications.

Data availability

The data will be available on request.

Conflicts of interest

The authors declare that there are no financial or any other conflicts of interests.

Acknowledgements

References

1 J. Li, M. Irfan, S. Samad, B. Ali, Y. Zhang, D. Badulescu and A. Badulescu, The relationship between energy consumption, CO$_2$ emissions, economic growth, and health indicators, *Int. Res. J. Publ. Environ. Health*, 2023, **20**(3), 2325.

2 W. F. Lamb, T. Wiedmann, J. Pongratz, R. Andrew, M. Crippa, J. G. Olivier, D. Wiedenhofer, G. Mattioli, A. A. Khourdajie, J. House, S. Pachauri, M. Figueroa, Y. Saheb, R. Slade, K. Haubacek, L. Sun, S. K. Ribeiro, S. Khennas, S. D. L. R. D. Can, L. Chapungu, S. J. Davis, I. Bashmakov, H. Dai, S. Dhakal, T. Tan, Y. Geng, B. Gu and J. Minx, A review of trends and drivers of greenhouse gas emissions by sector from 1990 to 2018, *Environ. Res. Lett.*, 2021, **16**(7), 073005.

3 R. Prăvălie, I. Sîrodoev, J. Ruiz-Arias and M. Dumitrașcu, Using renewable (solar) energy as a sustainable management pathway of lands highly sensitive to degradation in Romania. A countrywide analysis based on exploring the geographical and technical solar potentials, *Renewable Energy*, 2022, **193**, 976–990.

4 D. Bogdanov, A. Gulagi, M. Fasihi and C. Breyer, Full energy sector transition towards 100% renewable energy supply: Integrating power, heat, transport and industry sectors including desalination, *Appl. Energy*, 2021, **283**, 116273.

5 K. Ahmad, M. Q. Khan and H. Kim, Simulation and fabrication of all-inorganic antimony halide perovskite-like material based Pb-free perovskite solar cells, *Opt. Mater.*, 2022, **128**, 112374.

6 Y. Zhao, J. Zhu, B. He and Q. Tang, Dimensionality control of SnO$_2$ films for hysteresis-free, all-inorganic CsPbBr$_3$ perovskite solar cells with efficiency exceeding 10%, *ACS Appl. Mater. Interfaces*, 2021, **13**(9), 11058–11066.

7 G. Ding, Y. Zheng, X. Xiao, H. Cheng, G. Zhang, Y. Shi and Y. Shao, Sustainable development of perovskite solar cells: keeping a balance between toxicity and efficiency, *J. Mater. Chem. A*, 2022, **10**(15), 8159–8171.

8 S. Ullah, M. F. U. Din, J. Khan Kasi, A. Khan Kasi, K. Vegso, M. Kotlar, K. Micsuik, M. Jergel, V. Nadazdy, P. Siffalovic, E. Majkova and A. Fakharuddin, Mesoporous SnO$_2$ nanoparticle-based electron transport layer for perovskite solar cells, *ACS Appl. Nano Mater.*, 2022, **5**(6), 7822–7830.

9 S. T. Jan and M. Noman, Exploring the potential of MAGeI$_3$ perovskite cells with novel charge transport material optimization, *Optik*, 2024, **301**, 171684.

10 S. Guang, J. Yu, H. Wang, X. Liu, S. Qu, R. Zhu and W. Tang, A low temperature processable tin oxide interlayer via amine-modification for efficient and stable organic solar cells, *J. Energy Chem.*, 2021, **56**, 496–503.

11 P. Sakthivel, S. Foo, M. Thambidurai, P. C. Harikesh, N. Mathews, R. Yuvakkumar, G. Ravi and C. Dang, Efficient and stable planar perovskite solar cells using co-doped tin oxide as the electron transport layer, *J. Power Sources*, 2020, **471**, 228443.

12 K. Bhavsar and P. B. Lapsiwala, Numerical simulation of perovskite solar cell with different material as electron transport layer using SCAPS-1D software, *Semicond. Phys. Quantum Electron. Optoelectron.*, 2021, **24**(3), 341–347.

13 A. Uddin and H. Yi, Progress and challenges of SnO$_2$ electron transport layer for perovskite solar cells: A critical review, *Sol. RRL*, 2022, **6**(6), 2100983.

14 M. E. A. Boudia, Q. Wang and C. Zhao, Simulation and Comparison of the Photovoltaic Performance of Conventional and Inverted Organic Solar Cells with SnO$_2$ as Electron Transport Layers, *Energies*, 2024, **17**(13), 3302.

15 M. Singh, A. Ng, Z. Ren, H. Hu, H. C. Lin, C. W. Chu and G. Li, Facile synthesis of composite tin oxide nanostructures for high-performance planar perovskite solar cells, *Nano Energy*, 2019, **60**, 275–284.

16 Z. Xu, S. H. Teo, L. Gao, Z. Guo, Y. Kamata, S. Hayase and T. Ma, La-doped SnO_2 as ETL for efficient planar-structure hybrid perovskite solar cells, *Org. Electron.*, 2019, **73**, 62–68.

17 H. Yi, D. Wang, M. A. Mahmud, F. Haque, M. B. Upama, C. Xu, L. Duan and A. Uddin, Bilayer SnO_2 as electron transport layer for highly efficient perovskite solar cells, *ACS Appl. Energy Mater.*, 2018, **1**(11), 6027–6039.

18 N. Singh, A. Agarwal and M. Agarwal, Numerical simulation of highly efficient lead-free perovskite layers for the application of all-perovskite multi-junction solar cell, *Superlattices Microstruct.*, 2021, **149**, 106750.

19 H. Abdulsalam and G. Babaji, First principle study on lead-free $CH_3NH_3GeI_3$ and $CH_3NH_3GeBr_3$ perovskite solar cell using FHI-aims code, *J. Found. Appl. Phys.*, 2019, **6**(1), 76–88.

20 A. A. Kanoun, M. B. Kanoun, A. E. Merad and S. Goumri-Said, Toward development of high-performance perovskite solar cells based on $CH_3NH_3GeI_3$ using computational approach, *Sol. Energy*, 2019, **182**, 237–244.

21 Y. Q. Zhao, B. Liu, Z. L. Yu, J. Ma, Q. Wan, P. B. He and M. Q. Cai, Strong ferroelectric polarization of $CH_3NH_3GeI_3$ with high-absorption and mobility transport anisotropy: theoretical study, *J. Mater. Chem. C*, 2017, **5**(22), 5356–5364.

22 Y. Jiao, Y. Lv, J. Li, M. Niu and Z. Yang, Exploring electronic and optical properties of $CH_3NH_3GeI_3$ perovskite: Insights from the first principles, *J. Comput. Theor. Chem.*, 2017, **1114**, 20–24.

23 Y. Liu, The development of low toxic and high efficient solar cells, *J. Phys.: Conf. Ser.*, 2020, **1653**(1), 012002.

24 C. C. Stoumpos, L. Frazer, D. J. Clark, Y. S. Kim, S. H. Rhim, A. J. Freeman, J. B. Katterson, J. I. Jang and M. G. Kanatzidis, Hybrid germanium iodide perovskite semiconductors: active lone pairs, structural distortions, direct and indirect energy gaps, and strong nonlinear optical properties, *J. Am. Chem. Soc.*, 2015, **137**(21), 6804–6819.

25 S. Bhattarai and T. D. Das, Optimization of carrier transport materials for the performance enhancement of the $MAGeI_3$ based perovskite solar cell, *Sol. Energy*, 2021, **217**, 200–207.

26 H. Kuang and Y. Xiao, Numerical simulation of Cu_2Te based thin film solar cell with Cu_2O HTL for high efficiency, *Micro Nanostruct.*, 2024, **188**, 207790.

27 K. Chakraborty, N. R. Medikondu, P. B. Kanakavalli, V. V. Kamesh, S. Das, M. G. Choudhury and S. Paul, Comparative study of structural, opto-electronic properties of Cs_2TiX_6-based single halide double perovskite solar cells: computational and experimental approach, *Phys. Scr.*, 2024, **99**(10), 105554.

28 N. Kushwah, G. Kedarnath, A. Wadawale, K. K. Halankar, B. P. Mandal, M. Jafar and B. Vishwanadh, Molecular Precursor-Driven Synthesis of Copper Telluride Nanostructures for LIB Anode Application, *Inorg. Chem.*, 2023, **62**(23), 8823–8834.

29 S. R. Al Ahmed, M. Rahaman, A. Sunny, S. Rahman, M. S. Islam, T. A. E. M. Taha, Z. A. Alrowaili and M. S. Mian, Enhancing the efficiency of Cu_2Te thin-film solar cell with WS_2 buffer layer: a simulation study, *Opt Laser. Technol.*, 2023, **159**, 108942.

30 W. Henni, W. L. Rahal, G. I. Toki, M. K. Mohammed, L. B. Farhat, S. Ezzine, R. Pandey, A. Boukkortt and M. K. Hossain, Effect of adding Cu_2O as a back surface field layer on the performance of copper manganese tin sulfide solar cells, *Sustainability*, 2023, **15**(19), 14322.

31 R. Stangl, C. Leendertz and J. Haschke, Numerical simulation of solar cells and solar cell characterization methods: the open-source on demand program AFORS-HET, *Sol. Energy*, 2010, **14**, 319–352.

32 Y. Zhou and A. Gray-Weale, A numerical model for charge transport and energy conversion of perovskite solar cells, *Phys. Chem. Chem. Phys.*, 2016, **18**(6), 4476–4486.

33 P. J. Manga, M. Maina, H. Samaila, E. W. Likta, R. O. Amusat and S. Daniel, Exploring the structural mechanics of titanium nickel solid alloy using COMSOL Multiphysics: A Poisson equation and continuity equation perspective, *Sci. World J.*, 2024, **19**(1), 71–77.

34 A. Bablich, M. Müller, R. Bornemann, A. Nachtigal and P. Haring Bolívar, High responsivity and ultra-low detection limits in nonlinear a-Si: H pin photodiodes enabled by photogating, *Photonic Sens.*, 2023, **13**(4), 230415.

35 F. Brioua, C. Daoudi, B. Mekimah and B. Lekouaghet, The impact of a ZnO space layer on enhancing the efficiency of P3HT: PCBM blend-based organic solar cells, *Phys. Scr.*, 2024, **99**(8), 085951.

36 H. Asghar, T. Riaz, H. A. Mannan, S. M. Khan and O. M. Butt, Rheology and modeling insights into dye-sensitized solar cells (DSSCs) material: Bridging the gap to solar energy advancements, *Renew. Sustain. Energy Rev.*, 2024, **193**, 114298.

37 Z. Varga and E. Racz, Application development with finite element method to calculate photogeneration rate and open-circuit voltage of dye sensitized solar cell, *Theory Comput. Syst.*, 2022, **2**(2), 17–24.

38 T. Nakamura, W. Yanwachirakul, M. Imaizumi, M. Sugiyama, H. Akiyama and Y. Okada, Reducing Shockley–Read–Hall recombination losses in the depletion region of a solar cell by using a wide-gap emitter layer, *J. Appl. Phys.*, 2021, **130**, 153102.

39 A. Fell, T. Niewelt, B. Steinhauser, F. D. Heinz, M. C. Schubert and S. W. Glunz, Radiative recombination in silicon photovoltaics: Modeling the influence of charge carrier densities and photon recycling, *Sol. Energy Mater. Sol. Cells*, 2021, **230**, 111198.

40 Á. Nagy, I. Bodnár and E. Kovács, Simulation of the Thermal Behavior of a Photovoltaic Solar Panel Using Recent Explicit Numerical Methods, *Theor. Comput. Syst.*, 2024, **7**(7), 2400089.

41 M. Q. Kareem, S. A. Hassan, S. S. Alimardan, S. M. Shareef and M. M. Ameen, $CHTS/Zn_2P_3$-based solar cells with enhanced efficiency through ETL engineering: A numerical study, *J. Phys. Chem. Solids*, 2024, **188**, 111931.

42 G. Pindolia, S. M. Shinde and P. K. Jha, Optimization of an inorganic lead free $RbGeI_3$ based perovskite solar cell by SCAPS-1D simulation, *Sol. Energy*, 2022, **236**, 802–821.

43 S. Sakib, M. Y. M. Noor, M. R. Salim, A. S. Abdullah, A. I. Azmi, M. H. Ibrahim and M. H. Ibrahim, Effect of transport layer thickness in lead-based perovskite solar cell: A numerical simulation, *Mater. Today: Proc.*, 2023, **80**, 1022–1026.

44 A. Bag, R. Radhakrishnan, R. Nekovei and R. Jeyakumar, Effect of absorber layer, hole transport layer thicknesses, and its doping density on the performance of perovskite solar cells by device simulation, *Sol. Energy*, 2020, **196**, 177–182.

45 A. Mortadi, E. El Hafidi, M. Monkade and R. El Moznine, Investigating the influence of absorber layer thickness on the performance of perovskite solar cells: a combined simulation and impedance spectroscopy study, *Mater. Sci. Energy Technol.*, 2024, **7**, 158–165.

46 A. Ahmed, K. Riaz, H. Mehmood, T. Tauqeer and Z. Ahmad, Performance optimization of $CH_3NH_3Pb(I_{1-x}Br_x)_3$ based perovskite solar cells by comparing different ETL materials through conduction band offset engineering, *Opt. Mater.*, 2020, **105**, 109897.

47 B. K. Ravidas, A. R. Kumar, A. Praveen, S. K. Agnihotri, S. Bhattarai, R. Pandey, J. Madan, S. Singh, M. K. Hossain, M. K. Roy and D. P. Samajdar, Integration of SCAPS-1D and density functional theory for the performance evaluation of $RbGeI_3$-based perovskite solar cell, *J. Phys. Chem. Solids*, 2025, **196**, 112325.

48 R. Ranjan, N. Anand, M. N. Tripathi, N. Srivastava, A. K. Sharma, M. Yoshimura, L. Chang and R. N. Tiwari, SCAPS study on the effect of various hole transport layer on highly efficient 31.86% eco-friendly CZTS based solar cell, *Sci. Rep.*, 2023, **13**(1), 18411.

49 M. Mottakin, D. K. Sarkar, V. Selvanathan, M. J. Rashid, K. Sobayel, A. M. Hasan, M. A. Islam, G. Muhammad, M. Shahiduzzaman and M. Akhtaruzzaman, Photoelectric performance of environmentally benign Cs_2TiBr_6-based perovskite solar cell using spinel $NiCo_2O_4$ as HTL, *Optik*, 2023, **272**, 170232.

50 S. T. Jan and M. Noman, Influence of layer thickness, defect density, doping concentration, interface defects, work function, working temperature and reflecting coating on lead-free perovskite solar cell, *Sol. Energy*, 2022, **237**, 29–43.

51 S. A. Dar and B. S. Sengar, Analytical modeling and numerical investigation of grain size effects on polycrystalline perovskite based Thin-Film solar Cells: Performance insights and implications, *Sol. Energy*, 2025, **289**, 113313.

52 T. Kirchartz, High open-circuit voltages in lead-halide perovskite solar cells: experiment, theory and open questions, *Philos. Trans. R. Soc., A*, 2019, **377**(2152), 20180286.

53 A. Sachenko, V. Kostylyov and M. Evstigneev, Space charge region recombination in highly efficient silicon solar cells, *Semicond. Phys. Quantum Electron. Optoelectron.*, 2024, **27**(1), 010–027.

54 Q. Wang, S. Shao, B. Xu, H. Duim, J. Dong, S. Adjokatse, G. Portale, J. Hou, M. Saba and M. A. Loi, Impact of the hole transport layer on the charge extraction of Ruddlesden–Popper perovskite solar cells, *ACS Appl. Mater. Interfaces*, 2020, **12**(26), 29505–29512.

55 V. S. Chirvony, K. S. Sekerbayev, D. Perez-del-Rey, J. P. Martinez-Pastor, F. Palazon, P. P. Boix, T. I. Taurbayev, M. Sessolo and H. J. Bolink, Short photoluminescence lifetimes in vacuum-deposited $CH_3NH_3PbI_3$ perovskite thin films as a result of fast diffusion of photogenerated charge carriers, *J. Phys. Chem. Lett.*, 2019, **10**(17), 5167–5172.

56 S. Akel, A. Kulkarni, U. Rau and T. Kirchartz, Relevance of long diffusion lengths for efficient halide perovskite solar cells, *Phys. Rev. X Energy*, 2023, **2**(1), 013004.

57 I. Gulomova, O. Accouche, R. Aliev, Z. Al Barakeh and V. Abduazimov, Optimizing geometry and ETL materials for high-performance inverted perovskite solar cells by TCAD simulation, *Nanomaterials*, 2024, **14**(15), 1301.

58 A. Ren, H. Lai, X. Hao, Z. Tang, H. Xu, B. M. F. Y. Jeco, K. Watenabe, J. Zhang, M. Sugiyama, J. Wu and D. Zhao, Efficient perovskite solar modules with minimized nonradiative recombination and local carrier transport losses, *Joule*, 2020, **4**(6), 1263–1277.

59 D. Sahoo and N. B. Manik, Study on the effect of temperature on electrical and photovoltaic parameters of lead-free tin-based Perovskite solar cell, *Indian J. Phys.*, 2023, **97**(2), 447–455.

60 M. K. Hossain, M. A. Islam, M. S. Uddin, P. Paramasivam, J. A. Hamid, R. A. Alshgari, V. K. Mishra and R. Haldhar, Design and simulation of $CsPb_{.625}Zn_{.375}IBr_2$-based perovskite solar cells with different charge transport layers for efficiency enhancement, *Sci. Rep.*, 2024, **14**(1), 1–22.